Original Paper

Investigation of erosion-corrosion behavior of Q235B steel in liquid-solid flows

Yan-Lin Zhao [a, *], Fu-Xiang Ye [a], Ge Zhang [a], Jun Yao [a], Yu-Fa Liu [a], Shi-Gang Dong [b]

[a] International Joint Laboratory on Clean Energy Science and Technology, Beijing Key Laboratory of Process Fluid Filtration and Separation, College of Mechanical and Transportation Engineering, China University of Petroleum, Beijing, 102249, People's Republic of China
[b] College of Energy, Xiamen University, Xiamen, 361005, People's Republic of China

ARTICLE INFO

ABSTRACT

This work aims to investigate the erosion-corrosion behavior of Q235B steel in liquid-solid two-phase flows. The weight loss rate, surface morphology and electrochemical parameters of Q235B steel at different temperatures (20 °C, 30 °C, 40 °C) and flow velocities (6 m/s, 7 m/s, 8 m/s, 9 m/s, 10 m/s) were studied separately. The results show that the weight loss rate of Q235B steel specimens after erosion-corrosion increases with increasing flow velocity and temperature. For the erosion-corrosion process, the corrosion rates of specimens increase with increasing flow velocity. The results of surface morphology show that the circular pits with clear edges are distributed randomly over specimen surface at low flow velocity, but the pit edge becomes vague at high flow velocity. With temperature increasing, the erosion-corrosion damage became serious as shown by the aggregation of large and small pits on specimen surface. The working mechanism of erosion-corrosion is found to vary with flow velocity and temperature. The relationships among erosion-corrosion components are quantitatively represented and show that synergy dominates the progress of material loss. Corrosion enhances erosion that is a dominant component in the synergy. The inactions of erosion-corrosion can be described by "synergistic" and "additive" behavior. The results show that "additive" effect becomes more significant with increasing flow velocity but decreases with increasing temperature, while "synergistic" effect is not sensitive to flow velocity and temperature.

1. Introduction

Metal materials exposed to flowing corrosive fluid, especially in liquid-solid two-phase flow, usually suffer from erosion-corrosion (Wood, 2006). The mechanical erosion, caused by solid particles, and the electrochemical corrosion, caused by corrosive fluid, could promote each other and accelerate the degradation of materials due to the synergistic effect (Javaheri et al., 2018; Islam and Farhat, 2014; Zhao et al., 2015). Because of its complex mechanism, the erosion-corrosion behavior is not fully understood so far.

Due to the synergistic effect, the weight loss of metal material is often higher than the total weight loss caused by pure erosion and flow corrosion. The synergistic effect includes two parts: erosion enhanced corrosion and corrosion enhanced erosion (Liu et al., 2021; Shahali et al., 2019; Rajahram et al., 2009; Yang and Cheng, 2012; Guo et al., 2005). For erosion enhanced corrosion, the metal surface eroded by solid particles is easily corroded due to the damage of passive film or the formation of local defects (Rajahram et al., 2009; Yang and Cheng, 2012; Lu et al., 2011). For corrosion enhanced erosion, the anode current caused by corrosion could reduce the hardness of metallic materials and increase the weight loss of erosion, which has been confirmed by the study of Guo's (Guo et al., 2005). In addition, some researchers found that the occurrence of electrochemical reactions during corrosion process generates micro-current through charge transfer process (Xu and Tan, 2019; Xu et al., 2020). Therefore, the mechanical properties of materials could be changed, which could induce more weight loss of erosion.

The material loss caused by erosion-corrosion consists three main parts, which are pure erosion, flow corrosion and the synergistic effect (Shahali et al., 2019; Rajahram et al., 2009; Rameshk et al., 2020). Several factors could affect the erosion-corrosion

---

behavior of materials. The factors, which mainly affect the mechanical erosion, such as the particle parameters (Zhao et al., 2015, 2020; Kim et al., 2019), impact angle (Islam and Farhat, 2014; Xu et al., 2020; Zhao et al., 2020; Yao et al., 2015), flow velocity (Rameshk et al., 2020; Wang et al., 2019; Karafyllias et al., 2019) have been studied. Other factors, such as pH value (Stack and Pungwiwat, 2002; Owen et al., 2018), ionic environment (Aguirre et al., 2019; Stack et al., 2003), content of dissolved oxygen (Stack et al., 2003; Mahdi et al., 2014) and temperature (Mahdi et al., 2014; Elemuren et al., 2020) would mainly affect the erosion-corrosion behavior from the corrosion aspect. In these factors, flow velocity, which determines the kinetic energy of particle impact, has been proved to be one of the most common but essential factors in causing weight loss (Shahali et al., 2019; Zhao et al., 2020; Wang et al., 2019; Aguirre and Walczak, 2018; Guo et al., 2020). Elemuren et al. (2020) found that the influence of flow velocity is the most significant factor on erosion-corrosion rate by carrying out a full factorial, microscopic and spectroscopic study. The similar results were found by other researchers (Guo et al., 2020). It should be mentioned that the flow velocity not only relates to the mechanical erosion, but also influences the corrosion behavior by affecting the mass transfer process (Rajahram et al., 2009). However, the effect of flow velocity on corrosion pattern during erosion-corrosion has rarely been studied. Unlike the flow velocity, temperature, which is a common corrosion factor, is rarely studied in erosion-corrosion and there are some inconsistencies in the literatures. Aguirre and Walczak (2018) found that for X65 steel, temperature shows almost no influence on the total weight loss of material. However, Mahdi (Mahdi et al., 2014) found the surface morphology of X100 steel could be changed significantly by changing temperature. The influence of temperature on erosion-corrosion behavior is still unclear and need to be investigated furtherly.

Q235B steel is usually applied in marine environment (Xia et al., 2019; Zhang et al., 2021) and it's erosion-corrosion behavior is still not very clear. In this study, Q235B steel specimens were impinged by solid-liquid two phase flow. The effects of flow velocity and temperature on erosion-corrosion behavior of specimens were studied. Potentiodynamic polarization curve and electrochemical impedance spectroscopy (EIS) were used to investigate the corrosion performance. The weight loss measurement was carried out to obtain the weight losses of the specimens under different conditions. The surface morphology of specimens was studied by the confocal laser scanning microscope (CLSM) and scanning electron microscope (SEM).

In this work, jet device is used to study the erosion-corrosion behavior (Shahali et al., 2019; Rajahram et al., 2009; Yao et al., 2015). Compared with other experimental systems (Xu et al., 2020), its great advantage is able to well control the flow conditions such as impinging angle and velocity and obtain obvious loss of erosion-corrosion in a short time. As such, the working mechanism of erosion-corrosion can be analyzed and obtained.

2. Experimental details

2.1. Materials and specimen preparation

The chemical composition of Q235B steel samples used in this study is presented in Table 1. All of the samples were circular discs with the diameter of 15 mm and thickness of 2 mm. Fig. 1 shows the SEM pictures of the quartz sand particles used in this study, where particle shape is irregular with sharp edges and particle size ranges in 250–480 μm. The density of quartz sand is 2650 kg/m^3.

Before each test, the specimens were firstly polished by abrasive papers with 400, 800, 1200 grit, and then polished by 3.5 μm diamond polishing paste. The polished samples were washed by deionized water and acetone, followed by drying in air. After the experiment, the sample was cleaned in an ultrasonic cleaner for 3 min, and the surface of the sample was washed by deionized water. The weight losses of specimens before and after pure erosion and erosion-corrosion tests were measured using an analytical balance (Mettler Toledo) with accuracy of 0.1 mg. Each measurement was repeated three times.

2.2. Solid-liquid two phase flow

The solid-liquid two phase flow which was used in the study includes water, quartz sand and sodium chloride. The contents of quartz sand and sodium chloride change in the different experimental groups. There are three different experimental groups, which are called erosion-corrosion (E-C), pure erosion (E_0) and flow corrosion (C_0). The pure erosion tests were carried out using the two-phase flow containing distilled water and 0.5 wt% quartz sand. The erosion-corrosion tests were carried out using the solid-liquid two phase flow containing water, 0.5 wt% quartz sand and 3.5 wt% NaCl. The fluid used in the flow corrosion tests is water with 3.5 wt% NaCl. The duration of the pure erosion test (E_0) and erosion-corrosion test was 1 h.

The detailed test matrix is shown in Table 2, from which it can be seen that the experiments at temperatures of 20 °C, 30 °C and 40 °C were conducted under the velocity of 6 m/s, and the experiments at velocities of 6 m/s, 7 m/s, 8 m/s, 9 m/s, 10 m/s and 11 m/s were conducted under the temperature of 20 °C.

2.3. Experimental setup

The experiments were carried out using a submerged jet device as shown in Fig. 2. Based on previous work (Alam et al., 2016;

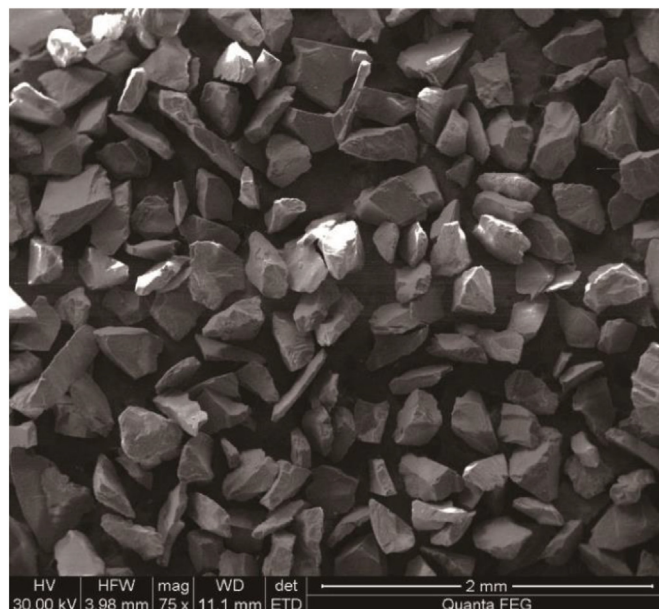**Fig. 1.** SEM micrographs of the quartz sand particles.

Table 1
Chemical composition of Q235B steel (mass fraction, %).

Material	C	Si	Mn	P	Al	Fe
Q235B	0.16	0.08	0.18	0.016	0.028	Bal.

Table 2
Testing matrix of Q235B steel samples.

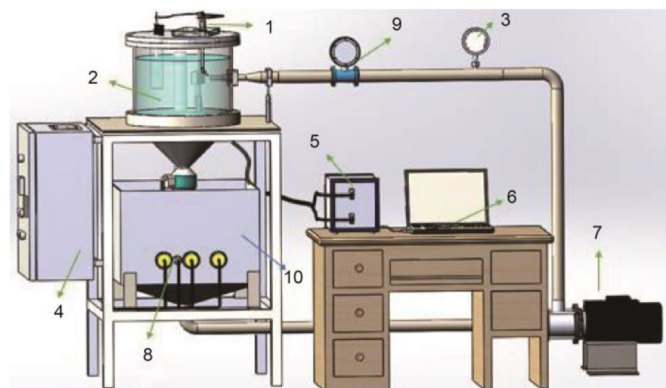| Groups		E_0	C_0	E-C
Temperature (°C) (6 m/s)	20	✓	✓	✓
	30	✓	✓	✓
	40	✓	✓	✓
Velocity (m/s) (20 °C)	6	✓	✓	✓
	7	✓	✓	✓
	8	✓	✓	✓
	9	✓	✓	✓
	10	✓	✓	✓
	11	✓	✓	✓

Fig. 2. Schematic of the jet device for erosion-corrosion. (1) electrochemical three-electrode measurement system; (2) plexiglass vessel; (3) pressure gauge; (4) control box; (5) electrochemical workstation; (6) computer; (7) pump; (8) temperature sensors; (9) flow meter; (10) water storage tank.

Rameshk et al., 2020), the nozzle distance was chosen as 3 cm in this work. The impact angle was set to be 90°. The nozzle diameter was set as 9 mm and the impinging jet can cover the whole area of the sample under the nozzle distance. The flow velocity and temperature were controlled by a frequency converter and an automatic temperature controller, respectively.

2.4. Electrochemical measurement

The electrochemical measurements were carried out on-line to characterize flow corrosion and erosion-corrosion. The samples were covered by epoxy resin except the working area 1 cm². The electrochemical measurements were conducted through three-electrode test system with a Reference 3000 electrochemical workstation (Gamry, America). Q235B steel sample was used as working electrode (WE), a platinum electrode was used as the counter electrode (CE) and a saturated calomel electrode (SCE) as the reference electrode (RE). Potentiodynamic polarization curve and electrochemical impedance spectroscopy (EIS) measurements were carried out during the flow corrosion and erosion-corrosion tests. The scan rate of potentiodynamic polarization curve was 0.3 mV/s. The electrochemical impedance spectroscopy tests were performed at open circuit potential with a sinusoidal potential excitation of 10 mV. The frequency was scanned from 100 kHz to 0.1 Hz (Laukkanen et al., 2020). The corrosion rate could be calculated by Eq. (1) (Liu et al., 2021).

$$\text{corrosion rate} = \frac{A \times i_{\text{corr}}}{n \times F \times \rho} \times 87600 \tag{1}$$

Where A is the atomic mass, i_{corr} is the corrosion current density (A/cm²), n is the number of electrons transferred by the

electrochemical reaction ($n = 2$), F is the Faraday constant ($1F = 26.8 A \cdot h$), and ρ is the density of the metal ($\rho = 7.85$ g/cm³).

2.5. Surface morphology characterization

The surface morphology of the samples was characterized using a three-dimensional confocal laser scanning microscope (CLSM) and a field emission scanning electron microscope (FESEM, FEI Quanta 200, Netherlands).

3. Results and discussion

3.1. Influence of flow velocity

3.1.1. wt loss of Q235B steel specimens after experiments

The weight loss of Q235B steel specimens after pure erosion, flow corrosion and erosion-corrosion at different flow velocities are presented in Fig. 3. It can be seen that after pure erosion and erosion-corrosion, the weight losses of Q235B steel specimens increase with increasing flow velocity, which means the higher flow velocity causes severer damage on metal materials in the both corrosive and non-corrosive media. The possible reason for this result is that the particles in the flow with high velocity could have high particle impact energy and therefore cause high material removal rate (Zhao et al., 2020; Yao et al., 2015; Alam et al., 2016). From Fig. 3, it can be also found that the weight losses of specimens caused by erosion-corrosion are larger than those after pure erosion at the same flow velocity. The degeneration of materials under the erosion-corrosion condition is worse than that under the pure erosion condition due to the synergistic effect of erosion-corrosion in the corrosive media.

3.1.2. Electrochemical measurement results during flow corrosion and erosion-corrosion

The corrosion rates of Q235B specimens during flow corrosion (C_0) and erosion-corrosion (E-C) processes were obtained from the potentiodynamic polarization curves by Tafel fitting. The potentiodynamic polarization curves at the different flow velocities under flow corrosion and erosion-corrosion conditions are shown in Fig. 4a-4b, respectively, and the Tafel fitting results are presented in
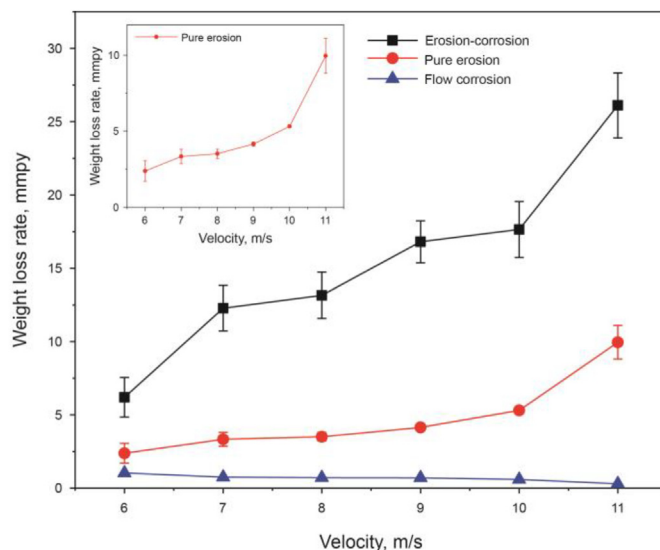

Fig. 3. wt loss of Q235B steel specimens at different velocities with a constant temperature value of 20 °C.

Table 3. It can be seen from Fig. 4 that the activation-passivation transition zone and pitting potentials are not shown in the potentiodynamic polarization curves, which indicates that the Q235B specimens are in the state of activated dissolution and without passivation during the experiments. Moreover, the corrosion potential shown in Fig. 4b shifts positively with the increasing of flow velocity, which could be the result of the increase of cathodic reaction rate because under erosion-corrosion condition, the transfer efficiency of the dissolved oxygen increases with the increasing velocity (Denny, 1996). From Tafel fitting results shown in Table 3, it can be seen that the corrosion currents density of specimens under the erosion-corrosion condition are greater than the corrosion currents density under the flow corrosion condition, which indicates the corrosion reaction is promoted under the erosion-corrosion process. It could be caused by the enhancement of the erosion on corrosion. Firstly, the impingement of solid particles on the surface of specimens can cause surface defects, such as craters, which are vulnerable to corrosion. Thus the local corrosion defects, such as pits could be produced due to the formation of anode area and corrosion galvanic cells around the craters (Xu and Tan, 2019). Secondly, with the flow velocity increasing, more fresh metal surfaces are exposed to the corrosive fluid due to the severer removal of the material and corrosion products, which could lead to the acceleration of the corrosion process of the materials.

In addition, Table 3 indicates that the averaged corrosion rates of specimens under the flow corrosion condition decrease with increasing flow velocity. Considering that no passivation behavior was found during tests and the Q235B steel is a nonpassive metal, this result is inconsistent with the general understanding that in a corrosive media, high flow velocity would cause high mass transfer efficiency and high corrosion rate (Denny, 1996). Hence, the possible reason could be related with the characteristics of the flow field which is called stagnant zone. In the single-phase flow, the stagnant zone in 90° impinging jets has been found by Tummers (Tummers et al., 2011) and Kalifa (Kalifa et al., 2016). Due to high pressure near the wall, the flow velocity becomes slow around the jet central area. So mass transfer may decrease with the low flow velocity and the corrosion process decreases as well. In this study, specimens are fixed at the center of the impinging area that is the stagnant zone. The influence of the stagnant zone could be the possible reason for the decrease of corrosion rate with increasing the flow velocity under the flow corrosion condition. For the erosion-corrosion process, the influence of the stagnant zone could be weakened, because the particles with initial kinetic energy

would still enter the stagnant zone and help to accelerate the mass transfer process by disturbing the flow field near the surface of the sample (Anderson and Longmire, 1995). Therefore, as shown in Table 3, the corrosion rate under the erosion-corrosion condition is larger than the one under the flow corrosion condition.

Fig. 5 presents the Nyquist plots and bode plots obtained for the Q235B steel specimens under the erosion-corrosion condition at different flow velocities. The equivalent circuit model is shown in Fig. 5a, where R_s is the solution resistance, R_{ct} is the charge transfer resistance, CPE_{dl} is the constant phase angle component used to describe the capacitance characteristic of non-ideal surfaces, n_{dl} ($0<n_{dl}<1$) is a parameter used to describe the CPE_{dl}, when $n_{dl} = 1$ the CPE_{dl} can be seen as an ideal capacitor (Amin et al., 2007). Table 4 shows the fitted equivalent circuit parameters of Q235B steel specimens. It can be seen from Fig. 5a that the diameters of capacitance arcs decrease with increasing flow velocities, which indicates a relatively low corrosion resistance and a high corrosion rate at high flow velocities. Fig. 5b presents the Bode plot, from which it can be seen that only one peak of phase angle exists indicating one time constant exists in each test result, and is also consistent with the single capacitance arc shown in Fig. 5a. In Table 4, the charge transfer resistances (R_{ct}) of specimens under the erosion-corrosion condition decrease with increasing the flow velocity. The charge transfer resistance reflects whether the corrosion of specimens is easy or not. Large R_{ct} means the corrosion rate of specimens is lower at the low flow velocity. Therefore, the EIS results show the same variation trend with the potentiodynamic polarization curves in Fig. 5b. The corrosion rates obtained from potentiodynamic polarization curves presented in Table 3 are reliable.

3.1.3. Surface morphologies

Fig. 6 shows the SEM micrographs of Q235B samples after pure erosion at flow velocities of 7 m/s, 9 m/s and 11 m/s. It can be seen that the surface morphology of specimens at different flow velocities is similar. The surfaces of specimens are covered with dense impact craters and indents, which is the typical surface morphology of specimens impinged at 90° (Javaheri et al., 2018). This result indicates that under the pure erosion condition, the effect of flow velocity on the particle impacting behavior is negligible.

Fig. 7 shows the SEM pictures of the Q235B specimens after erosion-corrosion at different flow velocities. It can be seen from Fig. 7 that the surface morphology of specimens shows two
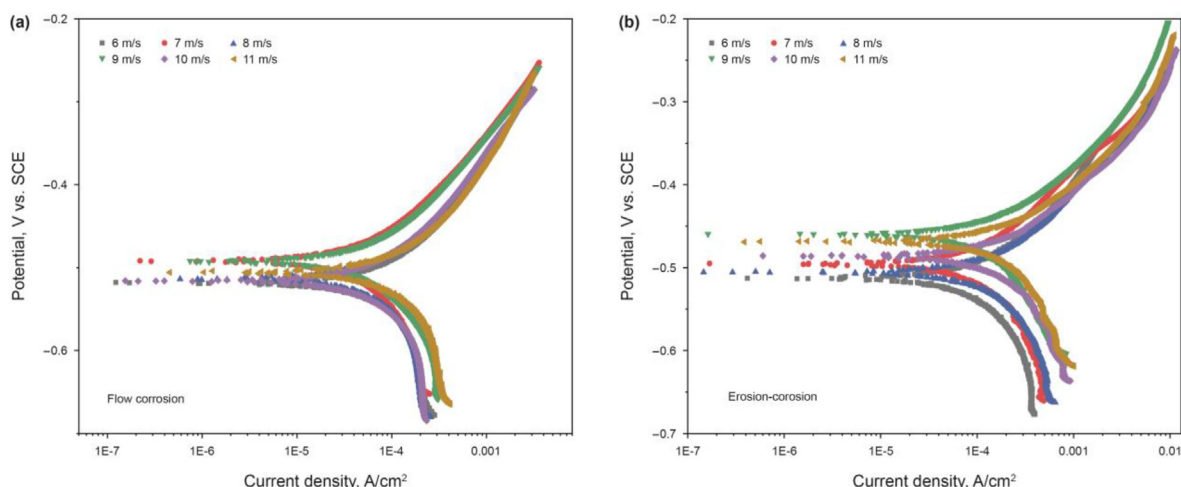

Fig. 4. Potentiodynamic polarization curves of Q235B steel at different velocities: (**a**) flow corrosion; (**b**) erosion-corrosion.

Table 3
Tafel fitting results of Q235B steel from potentiodynamic polarization curves (velocity).

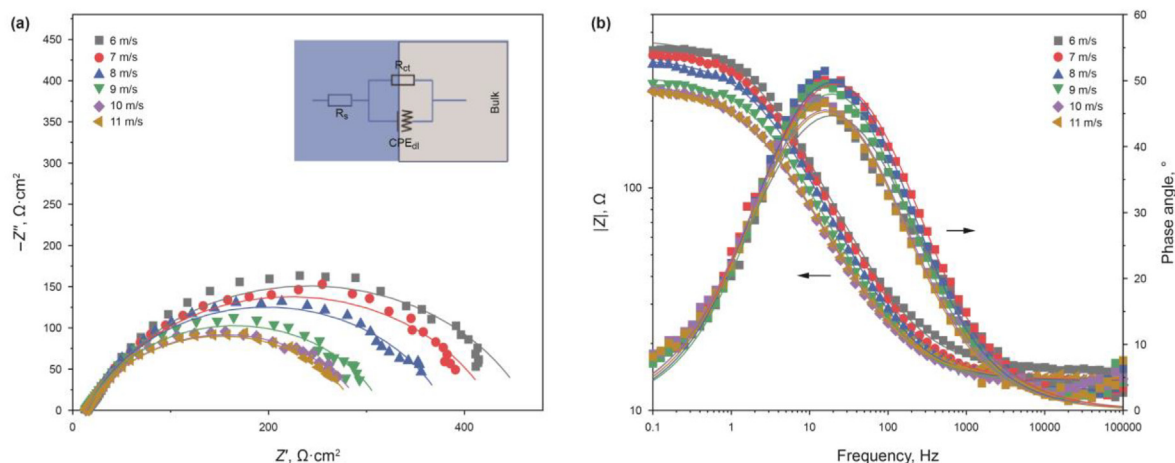| Flow velocity (m/s)	Testing condition	E_{corr}, mV	i_{corr}, A/cm^2	Corrosion rate, mmpy
6	C_0	−518.0	8.92×10^{-5}	1.025
	E-C	−512.0	1.63×10^{-4}	1.874
7	C_0	−492.0	6.53×10^{-5}	0.751
	E-C	−495.0	1.64×10^{-4}	1.886
8	C_0	−514.0	6.14×10^{-5}	0.706
	E-C	−505.0	1.75×10^{-4}	2.012
9	C_0	−496.0	6.07×10^{-5}	0.698
	E-C	−460.0	1.96×10^{-4}	2.253
10	C_0	−516.0	5.17×10^{-5}	0.599
	E-C	−486.0	2.51×10^{-4}	2.886
11	C_0	−505.0	2.60×10^{-5}	0.301
	E-C	−469.0	3.09×10^{-4}	3.553

Fig. 5. EIS of Q235B steel under erosion-corrosion condition at different velocities: (**a**) Nyquist plot; (**b**) Bode plot.

Table 4
Fitted equivalent circuit parameters of Q235B steel under the erosion-corrosion condition at different flow velocities.

Flow velocity (m/s)	R_s, Ω·cm^2	R_{ct}, Ω·cm^2	CPE_{dl}, Ω^{-1}cm^{-2}s^n	n_{dl}	Goodness of Fit
6	15.42	452.1	3.23×10^{-4}	0.750	2.80×10^{-3}
7	13.65	417.6	3.55×10^{-4}	0.743	7.92×10^{-4}
8	13.56	368.7	3.70×10^{-4}	0.760	1.33×10^{-3}
9	13.40	304.3	4.26×10^{-4}	0.756	1.55×10^{-3}
10	13.21	284.8	5.76×10^{-4}	0.728	1.45×10^{-3}
11	13.87	276.9	5.50×10^{-4}	0.734	1.28×10^{-3}

distinctive features. One is the regular indents and craters caused by particle impingement, the other is the corrosion pit which looks like dimples (Aguirre et al., 2019). The circular shaped pitting feature, formed under erosion-corrosion condition, is related to the joint effect of erosion and corrosion. It's worth mentioning that the circular pits with clear edges distributed randomly over the metal surface at the small flow velocities e.g. 6 m/s, 7 m/s, which is a common erosion-corrosion defect on the surface of carbon steels
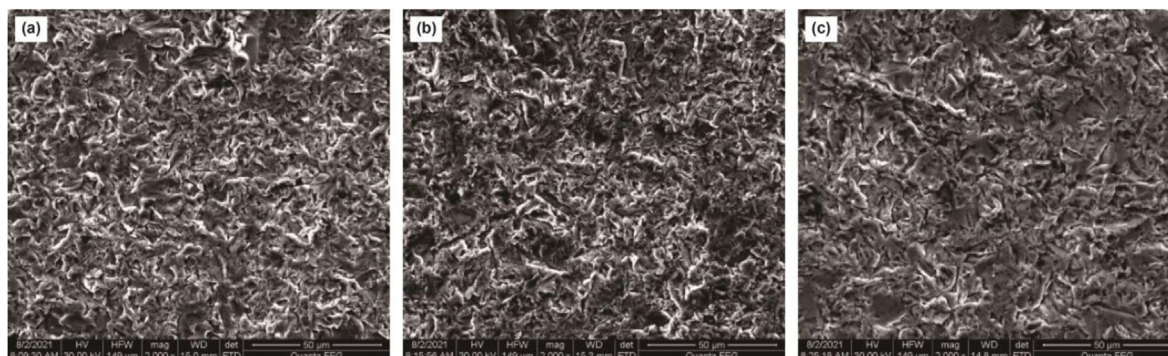

Fig. 6. SEM micrographs of Q235B samples after pure erosion: (**a**) 7 m/s; (**b**) 9 m/s; (**c**) 11 m/s.

under the vertical impingement (Islam and Farhat, 2014; Liu et al., 2021; Rameshk et al., 2020). However, at the high flow velocities e.g. 10 m/s and 11 m/s, the edge of the circular pits becomes vague. It can also be observed from Fig. 7 that at the velocities of 6 m/s and 7 m/s, most of the pits are circular, but with increasing of velocity, the shape of pits becomes irregular.

In order to further investigate the surface characters of Q235B specimens after erosion-corrosion at the different flow velocities, confocal laser scanning microscope (CLSM) was used to obtain the 3-D profiles of the surfaces of the specimens. Fig. 8 shows the three-dimensional topography of samples after erosion-corrosion at different flow velocities. As shown in Fig. 8, the surface damage can be obviously identified by the 3-D profiles. The scanning along the blue line (numbered by "(1)") represents the surface status without corrosion pits that can show the mechanical damage. The scanning

along the pink line (numbered by "(2)") aims to obtain the depth and width of corrosion pits. The larger the size of the corrosion pit, the more serious of the corrosion damage. The fluctuation of profiles along the blue line and pink line are shown in the pictures numbered by "(1)" and "(2)", respectively. After comparing the fluctuation of profiles without pits, it can be seen that at the flow velocities of 6 m/s, 7 m/s and 8 m/s, the fluctuation is small with range of 0—5 μm. When the flow velocity increases to 9 m/s, 10 m/s and 11 m/s, the fluctuation of profiles becomes larger and more than 5 μm, which means a serious surface damage due to the increasing of impact energy of particle collision under high flow velocity condition. Besides, it can be noticed from Fig. 8 that the depth of the corrosion pits decreases from 35.649 μm to 16.946 μm and the width of the corrosion pits decreases from 34.934 μm to 17.260 μm with increasing the flow velocity. These features imply
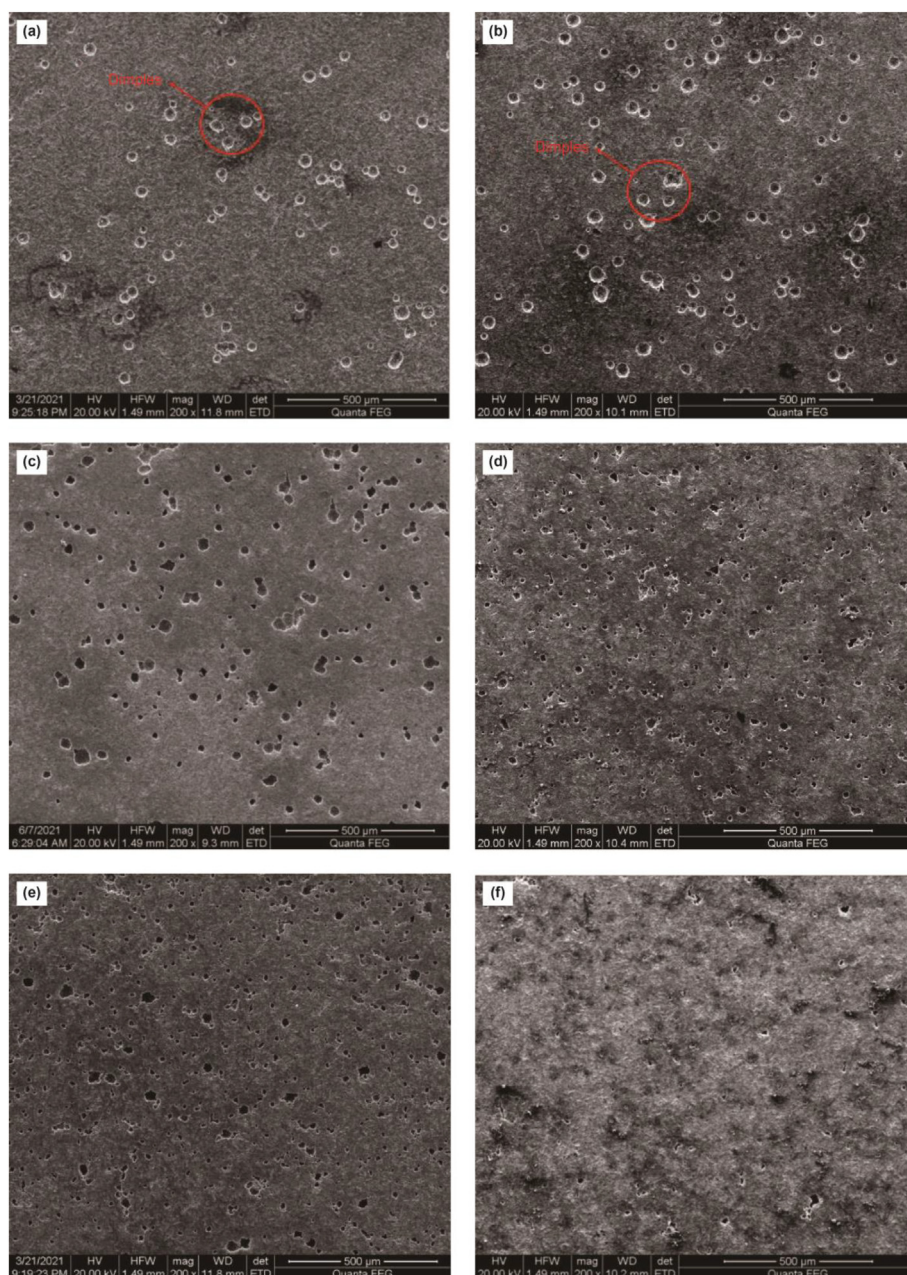

Fig. 7. SEM micrographs of Q235B samples under erosion-corrosion condition at velocities: (**a**) 6 m/s; (**b**) 7 m/s; (**c**) 8 m/s; (**d**) 9 m/s; (**e**) 10 m/s; (**f**) 11 m/s.
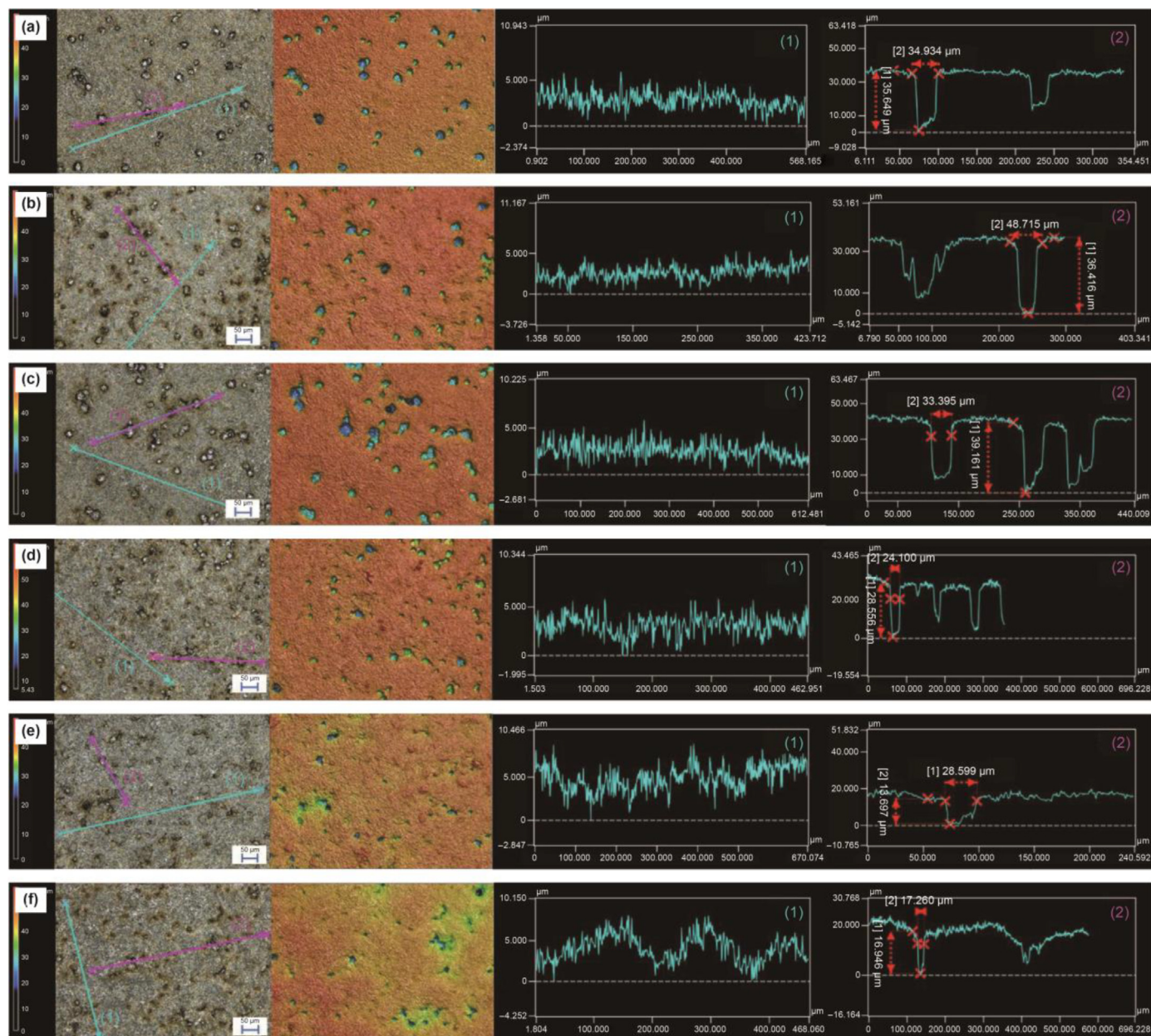
Fig. 8. CLSM photos of Q235B specimens under erosion-corrosion condition at different velocities: (**a**) 6 m/s; (**b**) 7 m/s; (**c**) 8 m/s; (**d**) 9.0 m/s; (**e**) 10.0 m/s; (**f**) 11.0 m/s.

the localized corrosion pattern of the Q235B specimens may have been changed with changing flow velocities. Considering the changing trend of surface profiles on the areas with and without corrosion pits, the erosion-corrosion behavior mechanism of Q235B steel under the effect of flow velocity is analyzed in next section.

3.1.4. Erosion-corrosion mechanism of Q235B steel: effect of flow velocity

It has been proved that with increasing flow velocity, the kinetic energy of the impinging particles increases as well, which could cause severe surface deformation and high material removal rate (Javaheri et al., 2018; Islam and Farhat, 2014; Sasaki and Burstein, 2000). Under the high impacting angle, the plastic deformation and flattening of ridges are the main mechanisms of particle erosion, fracture and vulnerable lips are thus formed and may break up and detach from the surface under subsequent particle collisions

(Alam et al., 2016). The continuous collision of particles will accelerate the removal of corrosion products on the surface of the specimens, so that the fresh surface could be exposed to the corrosive medium, which promotes the corrosion effectively (Wang et al., 2019; Li et al., 2019). Moreover, the defects like corrosion pits, which usually appear with the negative potential, could become anode and be preferentially corroded, while the surrounding area could become cathode and be protected (Xu and Tan, 2019). In this study, the influence of flow velocity on erosion-corrosion is mainly reflected in two aspects. On the one hand, at the high flow velocity, the weight loss caused by the mechanical erosion is larger than the one at the small flow velocity, which has been confirmed by the results of pure erosion and erosion-corrosion as shown in Fig. 3. On the other hand, the corrosion pattern during erosion-corrosion could be affected by the flow velocity, which can be seen from Fig. 6, where the characteristics of

corrosion defects (circular shaped pits) changed with increasing velocity. The corrosion pattern during erosion-corrosion under the different flow velocities would be focused. Fig. 9 is the schematic diagram of the surface deformation process of samples at low and high velocities, which shows the effect of flow velocity on corrosion pattern. Under the condition of small flow velocity, it is difficult to cause serious surface damage by the particle impingement due to the small kinetic energy of the impinging particles. Therefore, the small corrosion pits could be covered and protected by the corrosion products and be continuously developed into the large circular pits as shown in Fig. 7a–c. However, for large flow velocity, corrosion pits and their surrounding materials could be damaged or deformed seriously due to strong turbulence of local flow (Liu et al., 2021) carrying particles with high kinetic energy, which prevents corrosion pits from further developing. Therefore, the small and irregular shaped corrosion pits could be observed in Fig. 7e and f.

3.2. Influence of temperature

3.2.1. wt loss of Q235B steel specimens after E-C test

The weight loss results of Q235B steel specimens after pure erosion and erosion-corrosion, at different temperatures with a constant velocity of 6 m/s, are presented in Fig. 10. For pure erosion, there is no significant change in weight loss as shown in Fig. 10, when the temperature increases from 20 °C to 40 °C. However, for erosion-corrosion, the weight loss increases substantially as the temperature is increased. The possible reason for this result is that mechanical properties of Q235B steel would not be changed significantly in the temperature range of 20 °C–40 °C (Li et al., 2019), therefore the erosion behavior would not be affected by the change of temperature. However, the corrosion of specimens would be promoted by the increase of temperature (Mahdi et al., 2014; Slemnik, 2016). Thus, the weight losses of specimens after erosion-corrosion are increased with increasing temperature.

3.2.2. Electrochemical testing results during flow corrosion and erosion-corrosion

The potentiodynamic polarization curves, measured during the experiments, are shown in Fig. 11 and the fitting results are presented in Table 5. It can be found that the corrosion rates in both flow corrosion and erosion-corrosion increase with increasing temperature. Which means the corrosion of Q235B steel could be promoted at the high temperature. In addition, by comparing the corrosion rates measured under the flow corrosion and erosion-corrosion conditions at the same temperature, it can be seen obviously that the corrosion rates under erosion-corrosion condition are higher than those under the flow corrosion condition, which means the particles in the fluid promote the corrosion
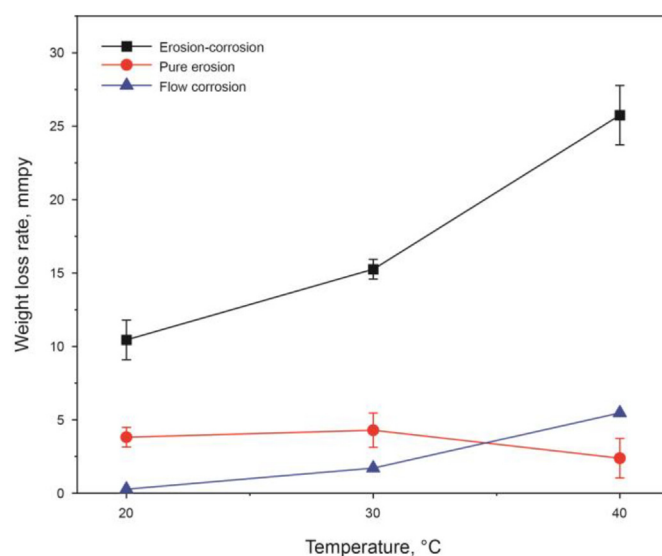

Fig. 10. wt loss of Q235B steel specimens at different temperatures with a constant flow velocity of 6 m/s.

process of specimens. It is worth mentioned that the corrosion rates for flow corrosion at 40 °C (5.468 mmpy) is significantly greater than those under erosion-corrosion condition at 20 °C and 30 °C, which means flow corrosion is more susceptible to temperature than erosion-corrosion.

Fig. 12 presents the EIS results of Q235B steel at different temperature under the flow corrosion and erosion-corrosion condition and the fitted equivalent circuit parameters of specimens are shown in Table 6. Fig. 11a shows that the diameters of capacitance arcs decrease with the increase of temperature under the flow corrosion and erosion-corrosion conditions. Besides, the charge transfer resistance R_{ct} decreases significantly with increasing temperature as shown in Table 6. These results reflect that the corrosion becomes severer when the temperature is increased. It has been proved that the activation energy of corrosion reaction can be reduced when temperature is increased (Slemnik, 2016), therefore, the corrosion reaction could be happened easily and the corrosion resistance of specimens would be reduced. Moreover, in Fig. 12a and b, two capacitance arcs could be found in Nyquist plot and two times constants found in Bode plot at 40 °C, which indicated that various phenomenon happened. The time constant at low frequencies (from 1 to 10 Hz) might relate to the ionic transport process through surface and the other one could associate with the impedance related to corrosion products formed at the sample
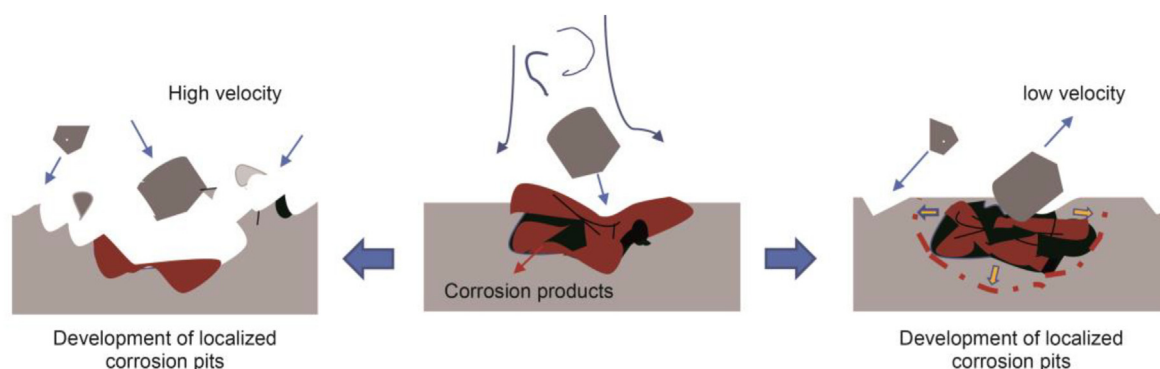

Fig. 9. Schematic diagram of material surface damage at low and high flow rates.
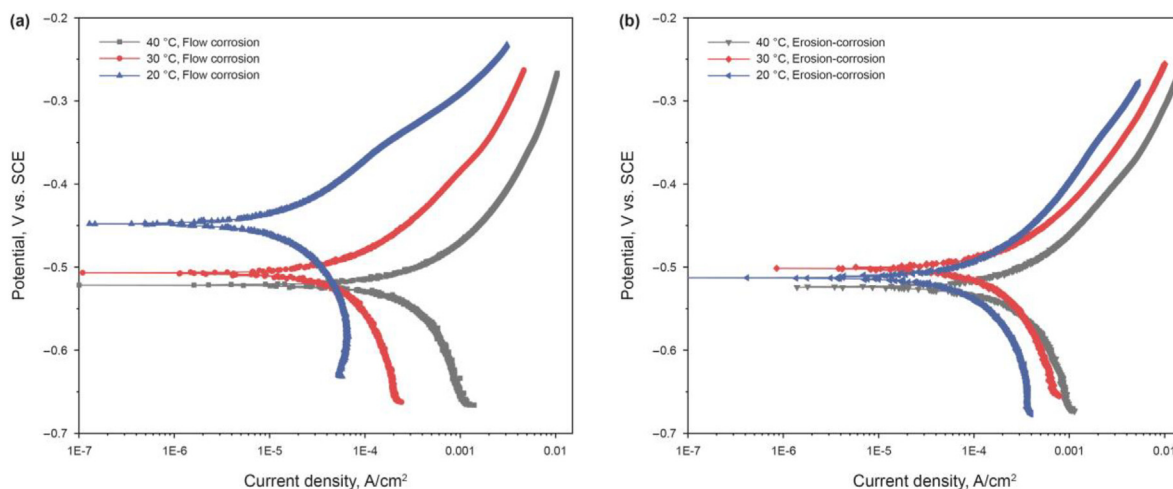
Fig. 11. Potentiodynamic polarization curves of Q235B steel at different temperatures: (**a**) flow corrosion; (**b**) erosion-corrosion.

Table 5
Tafel fitting results of Q235B steel from potentiodynamic polarization curves (temperature).

Temperature, °C	Testing condition	E_{corr}, mV	i_{corr}, A/cm^2	Corrosion rate, mmpy
20	C_0	−518.0	8.92×10^{-5}	1.026
	E-C	−512.0	1.63×10^{-4}	1.874
30	C_0	−507.0	1.48×10^{-4}	1.702
	E-C	−505.0	3.77×10^{-4}	4.335
40	C_0	−522.0	4.71×10^{-4}	5.416
	E-C	−524.0	5.47×10^{-4}	6.290

surface (Hirata et al., 2021). As such, the equivalent circuit model at 40 °C was different with those at 20 °C and 30 °C. Fig. 12c shows the equivalent circuit model for the specimens tested at 20 °C and 30 °C, which is the same as Fig. 5. Fig. 12d shows the equivalent circuit model for the specimens tested at 40 °C, where R_s is the solution resistance, R_{ct} is the charge transfer resistance, R_{pro} is the corrosion product resistance, CPE_{pro} is the capacitance of corrosion product, CPE_{dl} is the electric double-layer capacitance.

3.2.3. Surface morphology measurement

Fig. 13 shows the surface morphologies of the samples after pure erosion at different temperatures. It can be seen that the surface is dominated by large area of the indention and particle impact craters. The surface morphology of specimens at different temperature is almost the same. Considering the weight loss results showed in Fig. 10, it can be deduced that the change of temperature, from 20 °C to 40 °C, have no noticeable effects on pure erosion. The possible reason is that the mechanical properties of the Q235B steel would not be changed significantly in the range of 20 °C–40 °C (Molkens et al., 2021).

However, the characteristics of specimen surface are quite different after erosion-corrosion tests at different temperatures as shown in Fig. 14. It can be seen from Fig. 14a–c that at 20 °C, circular shaped corrosion pits randomly distribute on the surface of the sample, while at 30 °C, less but larger pits can be seen. Interestingly, these pits seem to have a trend of interconnection, especially at 40 °C, which means the corrosion pits might have a regional aggregation characteristic when the temperature is increased. Xu (Xu et al., 2020) claimed that corrosion initiated on small anodic sites which randomly appeared on the surface due to the inhomogeneous material defects, for example particle impact craters. Those small anodic sites are more susceptible to corrosion compared to the area adjacent to them, therefore, the anodic sites would be

corroded preferentially and the surrounding area could be protected as the cathode.

In Fig. 14e, a few large corrosion pits can be seen and some small corrosion pits are around these large pits to form a cluster. Thus, it can be confirmed that the preferential corrosion area exists during erosion-corrosion of Q235B steel and the initial anodic sites could have one or more cores of those defects inside. With the increase of temperature from 20 °C to 30 °C, the corrosion pits become large, which is probably caused by the acceleration of pitting pits corrosion (Mahdi et al., 2014). At 40 °C, many small and large corrosion pits can be seen observed on the surface, as shown in Fig. 14c and f. The significant increase in the number of pitting pits is possibly due to the promotion of corrosion with the increase of temperature.

In order to study the size of corrosion pit quantitatively, the confocal laser scanning microscope (CLSM) pictures were measured and analyzed. Fig. 15 presents the CLSM photos of Q235B specimens under erosion-corrosion at different temperatures. It is seen that the pits are small in size and distribute evenly at the sample surface at 20 °C. The pit size tends to increase gradually at 30 °C. As the temperature reaches 40 °C, large pits seem to keep constant as that at 30 °C while small pits tend to distribute around large ones. Similar results can be found in Fig. 14. Based on the profiles measured by CLSM, more detail about the surface including width and depth of corrosion pits could be characterized. The blue line (numbered by "(1)") represents the variation of the surface profile without pits, while the pink one (numbered by "(2)") indicates the depth and width of the corrosion pits. The fluctuation of the blue and pink profiles is shown in Fig. 15 and numbered with "(1)" and "(2)", respectively. It is seen that the fluctuation of the blue profile at 20 °C, 30 °C and 40 °C is similar to each other, and approximately within 5 μm. As shown in Fig. 15, at 20 °C the width and depth of the corrosion pits are 34.9 μm and 35.6 μm, respectively; at 30 °C it increases as 103.5 μm and 51.2 μm, respectively
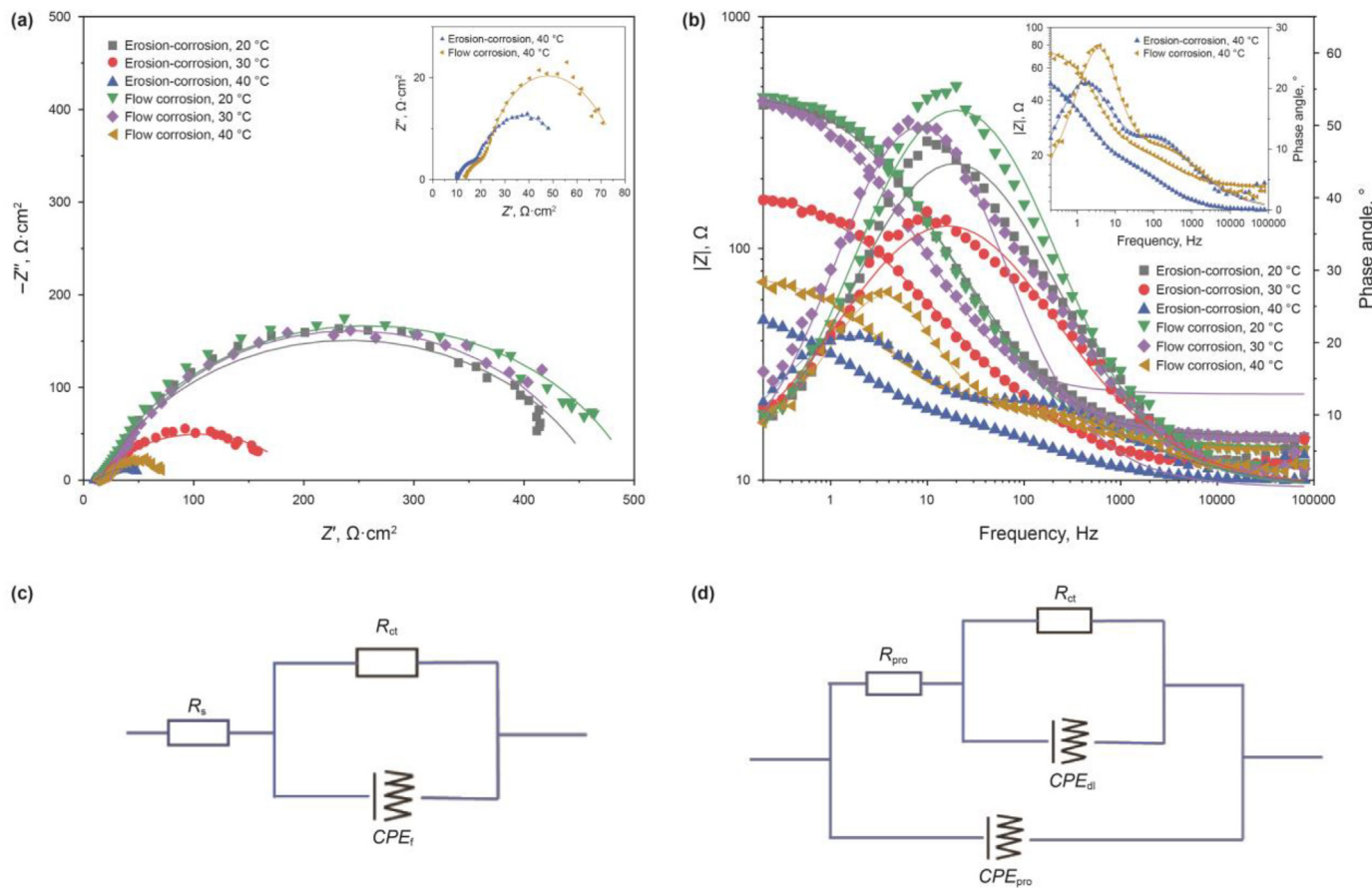
Fig. 12. EIS of Q235B steel under flow corrosion and erosion-corrosion conditions at different temperatures: (**a**) Nyquist plot; (**b**) Bode plot; (**c**) Equivalent circuit for EIS fitting under 20 °C and 30 °C; (**d**) Equivalent circuit for EIS fitting under 40 °C.

Table 6
Electrochemical parameters of Q235B steel under flow corrosion and erosion-corrosion at different temperatures.

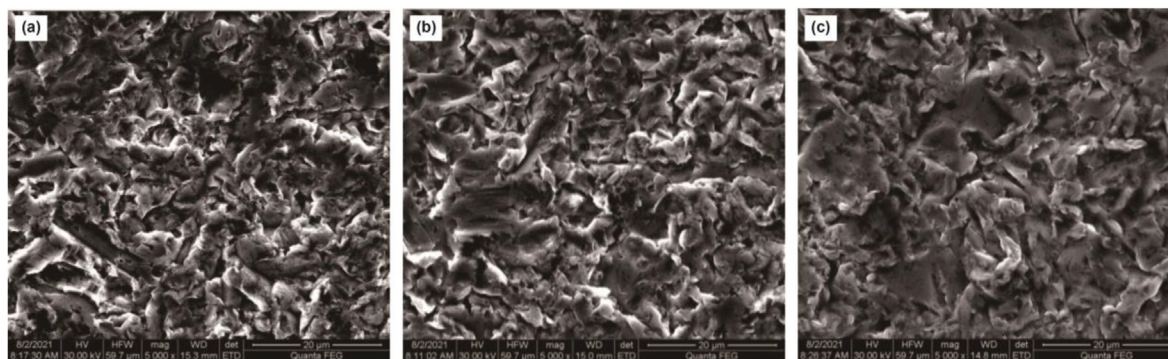| Test conditions, °C		R_s, $\Omega \cdot cm^2$	R_{pro}, $\Omega \cdot cm^2$	R_{ct}, $\Omega \cdot cm^2$	CPE_{pro}, $\Omega^{-1}cm^{-2}s^n$	CPE_{dl}, $\Omega^{-1}cm^{-2}s^n$	N_{pro}	N_{dl}	Goodness of Fit
20	C_0	13.92		486.8	3.07×10^{-4}		0.764	–	2.85×10^{-3}
	E-C	15.42	–	452.1	3.23×10^{-4}		0.750	–	$2.80 \times 10\text{-}3$
30	C_0	23.49	–	439.5	4.13×10^{-4}	–	0.806	–	1.49×10^{-4}
	E-C	11.43	–	185.9	1.26×10^{-3}	–	0.623	–	1.55×10^{-3}
40	C_0	12.94	15.38	53.95	2.24×10^{-3}	1.39×10^{-3}	0.545	0.925	1.13×10^{-4}
	E-C	9.91	10.48	37.89	1.83×10^{-3}	8.28×10^{-3}	0.625	0.711	8.74×10^{-5}

Fig. 13. SEM photos Q235B steel surface after pure erosion at different temperatures: (**a**) 20 °C; (**b**) 30 °C; (**c**) 40 °C.
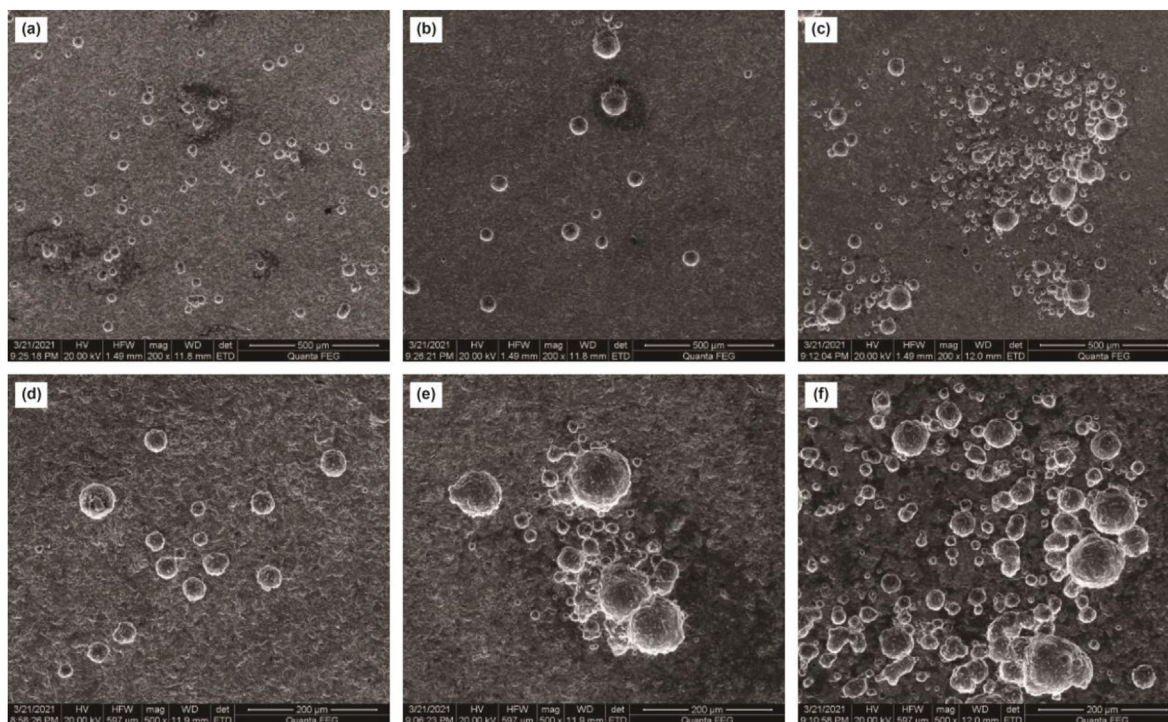
Fig. 14. SEM photos Q235B steel surface after erosion-corrosion at different temperatures: (**a**), (**d**) 20 °C; (**b**), (**e**) 30 °C; (**c**), (**f**) 40 °C.
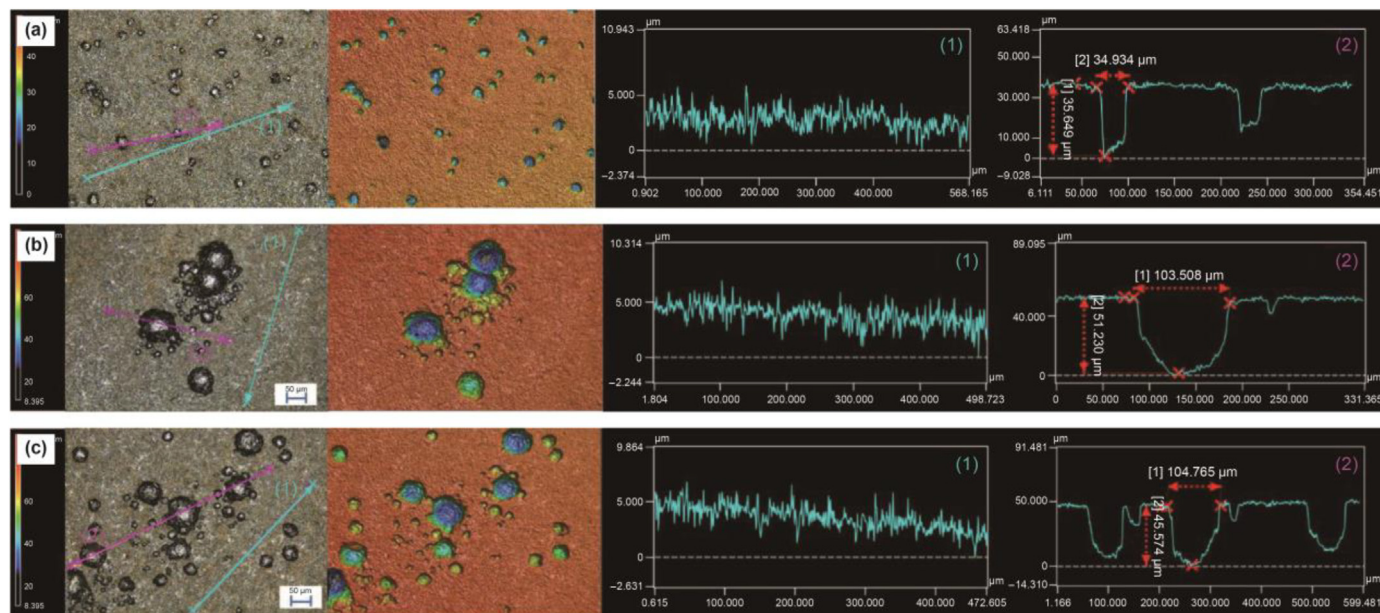

Fig. 15. CLSM photos of Q235B specimens under erosion-corrosion condition at different temperatures: (**a**) 20 °C; (**b**) 30 °C; (**c**) 40 °C.

and at 40 °C, it reaches as 104.8 μm and 45.6 μm, respectively. It is seen that the size and depth of corrosion pit are increased with increasing temperature, although such increment is small from 30 °C to 40 °C. It is suggested that the corrosion pits can be further developed. Moreover, as the temperature reaches 40 °C, though the size of large pits is close to that at 30 °C, more small pits appear around large ones. Such variation trend can be seen in Fig. 14 as well.

3.2.4. Erosion-corrosion mechanism of Q235B steel under the effect of temperature

In general, the effect of temperature on erosion-corrosion behavior of Q235B steel includes two aspects. Firstly, the increase of temperature leads to a significant increase in weight loss through corrosion enhanced erosion. Secondly, under the different temperature conditions, the corrosion pits show different distribution characteristics on the surface of specimens.
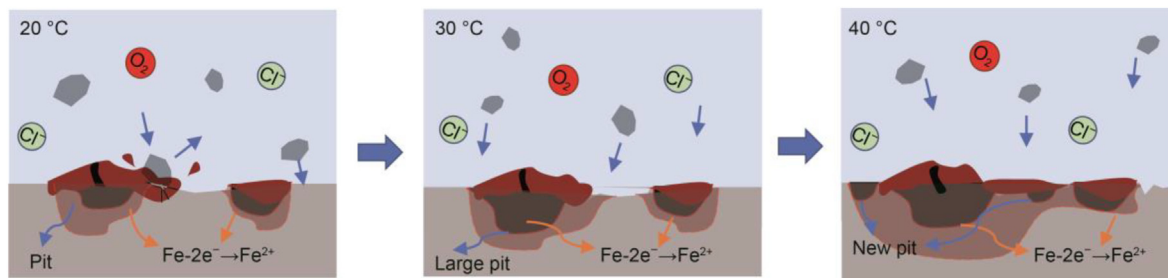
Fig. 16. Schematic diagrams of the pitting characteristics at different temperatures.

In an oxygen containing NaCl solution, the main corrosion reaction can be listed as following (Xu and Tan, 2019; Elemuren et al., 2020).

Anodic reaction:

$$Fe \rightarrow 2e^- + Fe^{2+} \tag{2}$$

Cathodic reaction:

$$O_2 + 2H_2O + 4e^- \rightarrow 4OH^- \tag{3}$$

Net reaction:

$$Fe^{2+} + 2H_2O \rightarrow Fe(OH)_2 + 2H^+ \tag{4}$$

In general, the ferrous ions come from the anodic dissolution of the metal and hydrolyze to form ferrous hydroxide and hydrogen ion. As the hydroxide accumulate on an anode site, the diffusion of the hydrogen and hydroxide ions would decrease due to the corrosion product. It may increase local high pH and generate more pits. Although chloride ions cannot be seen in the reactions, the anodic dissolution increases due to its high adsorption and electronegativity (Mccafferty, 1990). Furthermore, as ferrous ions generate inside the pits, chloride ions would migrate from the external solution toward inside the pits and maintain the electrical neutrality (Liu et al., 2021). It may cause some difference of the solution concentration between inside and outside of pits.

Fig. 16 shows the variation process of the sample surface at different temperatures (20 °C, 30 °C and 40 °C), which indicates the effect of temperature on the erosion-corrosion process of Q235B steel. As the temperature is as low as 20 °C, the corrosion pit distributes evenly on the surface and its size is small. As the temperature increases as 30 °C, the number of pits increases and they form a large regional anode area where each stable pit works as the core. Under the combined effect of low pH and high concentration of chloride ions, the metal around the pits becomes vulnerable and causes more pits to generate. As temperature increases higher, the area of corrosion pit become wider at 40 °C.

3.3. Analysis of erosion-corrosion components

In order to analyze the effects of erosion, corrosion and synergy behavior on the weight loss and investigate their inner relation, the analysis of erosion-corrosion components was carried out. The total erosion-corrosion rate could be divided into three parts according to the following equations (Yang and Cheng, 2012):

$$T = C_0 + E_0 + S \tag{5}$$

$$S = C_e + E_c \tag{6}$$

where T is the total erosion-corrosion rate, C_0 is the flow corrosion

Table 7
Erosion-corrosion parameters of Q235B steel in 3.5% NaCl solution containing 0.5 wt% SiO$_2$ particles at different flow velocity (unite: mm/year).

Flow velocity	T	E_0	C_0	S	C_w	C_e	E_c	E_w
6 m/s	6.2	2.384	1.026	2.790	1.874	0.848	1.942	4.326
percentage in T, %	–	38.45%	16.55%	45.00%	30.23%	13.68%	31.32%	69.77%
7 m/s	12.28	3.338	0.751	8.191	1.886	1.135	7.056	10.377
percentage in T, %	–	27.18%	6.12%	66.70%	15.36%	9.24%	57.46%	84.50%
8 m/s	13.154	3.517	0.706	8.931	2.012	1.306	7.625	11.119
percentage in T, %	–	26.74%	5.37%	67.90%	15.30%	9.93%	57.97%	84.53%
9 m/s	16.81	4.149	0.698	11.963	2.253	1.555	10.408	14.531
percentage in T, %	–	24.68%	4.15%	71.17%	13.40%	9.25%	61.92%	86.44%
10 m/s	17.645	5.305	0.599	11.741	2.886	2.287	9.454	14.737
percentage in T, %	–	30.07%	3.39%	66.54%	16.36%	12.96%	53.58%	83.52%
11 m/s	26.11	9.955	0.301	15.854	3.553	3.252	12.602	22.518
percentage in T, %	–	38.13%	1.15%	60.72%	13.61%	12.45%	48.27%	86.24%

Table 8
Erosion-corrosion parameters of Q235B steel in 3.5% NaCl solution containing 0.5 wt% SiO$_2$ particles at different temperature (all units are in mm/year).

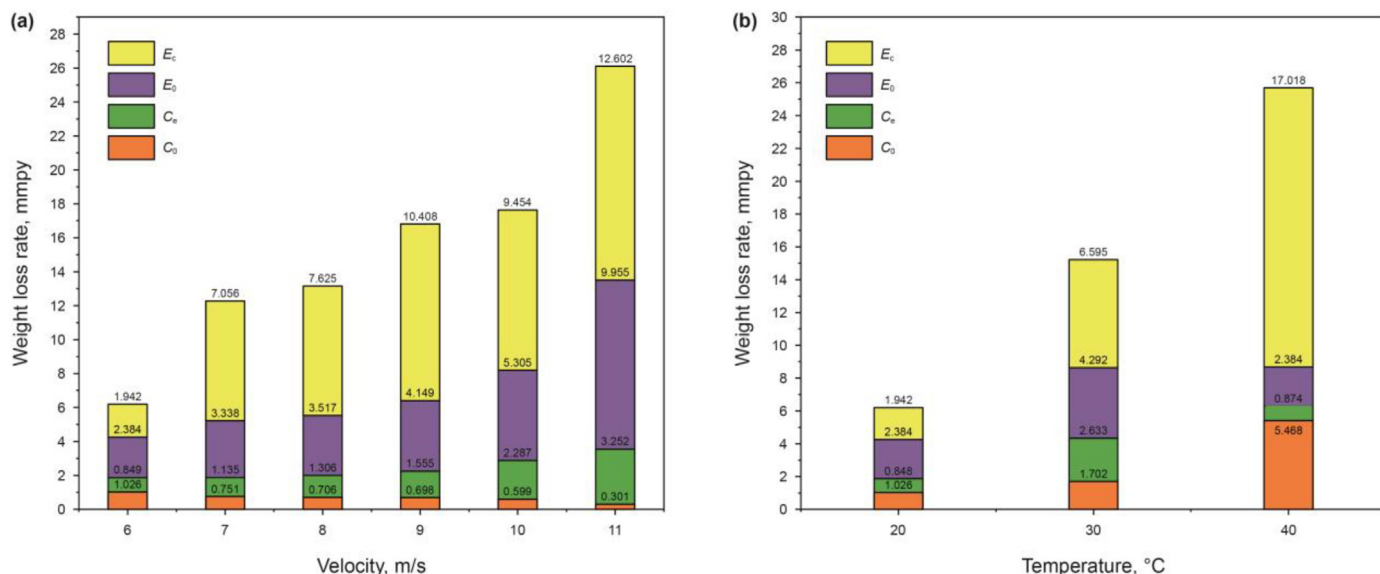| Temperature (°C)	T	E_0	C_0	S	C_w	C_e	E_c	E_w
20	6.2	2.384	1.026	2.790	1.874	0.848	1.942	4.326
percentage in T, %	–	38.45%	16.55%	45.00%	30.23%	13.68%	31.05%	69.77%
30	15.26	4.292	1.702	9.266	4.335	2.633	6.595	10.925
percentage in T, %	–	28.13%	11.15%	60.72%	28.41%	17.25%	43.22%	71.59%
40	25.752	2.384	5.416	17.952	6.290	0.874	17.018	19.462
percentage in T, %	–	9.26%	21.03%	69.71%	24.43%	3.39%	66.08%	75.57%

Fig. 17. wt loss rate of Q235B steel caused by corrosion enhanced erosion (E_c), pure-erosion (E_0), erosion enhanced corrosion (C_e) and flow corrosion (C_0) at different flow velocities and temperatures: (**a**) flow velocity (**b**) temperature.

rate in the absence of erosion, E_0 is the pure erosion rate in the absence of corrosion, S is the synergy which contains the erosion enhanced corrosion (C_e) and corrosion enhances erosion (E_c). Since T, C_0 and E_0 could be derived from the experiment of erosion-corrosion, flow corrosion and pure erosion, respectively, the weight loss rate caused by synergy S could be calculated from Eq. (5). However, C_e and E_c are unknown. In order to obtain the value of C_e and E_c, following equations are necessary:

$$C_w = C_e + C_0 \tag{7}$$

$$E_w = E_c + E_0 \tag{8}$$

where C_w is the total corrosion rate, E_w is the total erosion rate. C_w can be derived from Tafel fitting using potentiodynamic polarization curves measured during erosion-corrosion tests. C_0 can be obtained from the experiment of flow corrosion, therefore, C_e can be calculated from Eq. (7). Once C_e is available, E_c can be calculated by Eq. (3). At last, E_w can be calculated by Eq. (8). Combining Eqs. (5)–(8), the total erosion-corrosion rate (T) can be represented by the sum of two parts, E_w and C_w as shown in the following:

$$T = E_w + C_w \tag{9}$$

Table 7 and Table 8 present the erosion-corrosion components (expressed in millimeter per year) of Q235B steel in 3.5% NaCl solution containing 0.5 wt% quartz particles at different flow velocity and different temperature, respectively. It can be seen from Tables 7 and 8 that synergy (S) is the main reason for causing massive material loss among erosion-corrosion tests, because the percentage of synergy (S) in the total erosion-corrosion rate (T) is high (from 45.0% to 71.17%), which is larger than the percentage of flow corrosion rate (C_0) and percentage of pure erosion (E_0).

Fig. 17 presents the weight loss rate of Q235B steel caused by corrosion enhanced erosion (E_c), pure erosion (E_0), erosion enhanced corrosion (C_e) and flow corrosion (C_0) at different flow velocities and temperatures. From Fig. 17, it can be seen that corrosion enhanced erosion rate (E_c) is the dominant component of synergy in most erosion-corrosion experiments. In addition, with increase of flow velocity, both corrosion enhanced erosion rate (E_c)

and erosion enhanced corrosion rate (C_e) of Q235B samples are promoted as shown in Fig. 16a. However, it can be seen from Fig. 17b that the erosion enhanced corrosion rate C_e is not increased with increasing temperature which means that C_e is not sensitive to temperature. It seems possible because temperature doesn't have direct effect on the erosion and flow velocity as shown in pure erosion tests. With increasing temperature, corrosion enhanced erosion rate (E_c) increases significantly as shown in Fig. 17b, which is possibly due to the increase of corrosion rate. With increasing corrosion rate, the surface of specimens becomes loose due to the cover of corrosion products, which is easily removed by the impingement of particles and relatively large weight loss could be obtained. This result is consistent with those from literature (Shahali et al., 2019; Abedini and Ghasemi, 2014).

In order to investigate the quantitative relationship between erosion and corrosion, the erosion-corrosion map was used as the
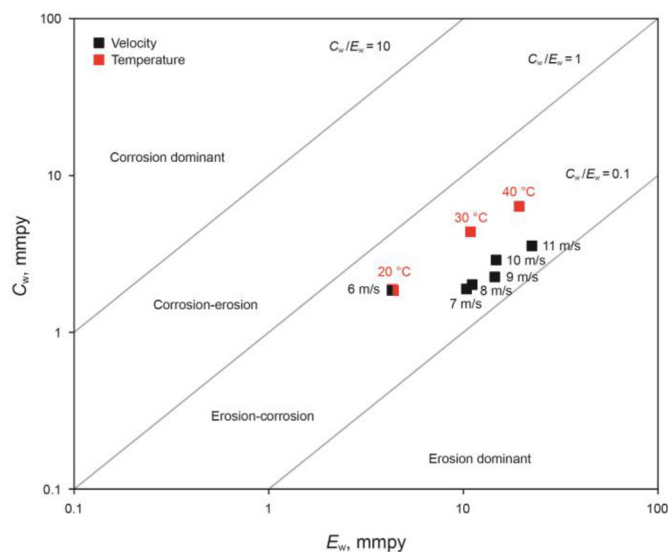

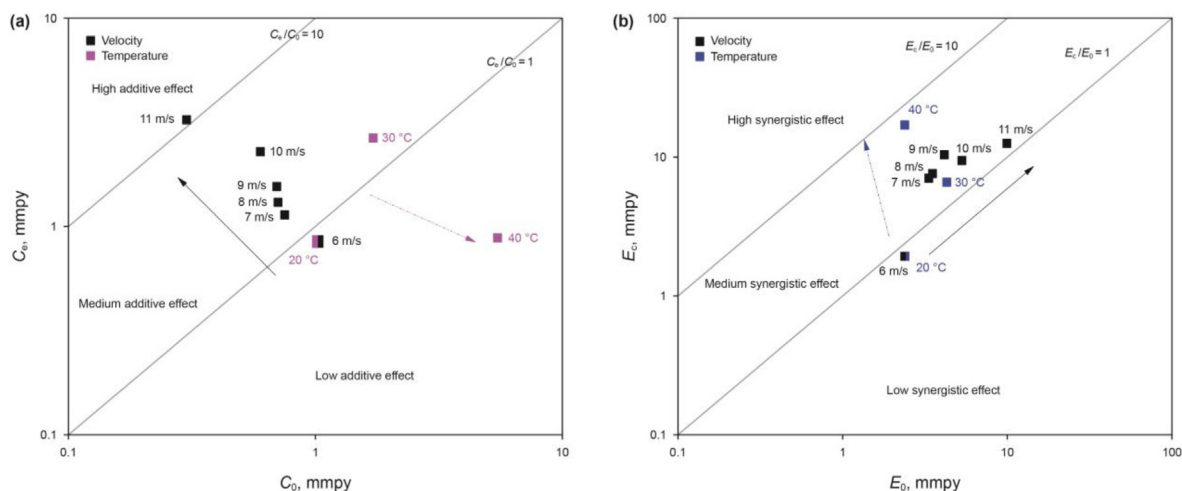**Fig. 18.** Erosion-corrosion map of Q235B steel at different flow velocities and temperatures.

Fig. 19. Erosion-corrosion additive and synergistic behavior maps: (**a**) additive effect and (**b**) synergistic effect.

ratio of erosion rate (E_w) to corrosion rate (C_w), which can compare both effects directly. Based on previous work (Rajahram et al., 2009; Yang and Cheng, 2012), the ratio can be divided into four regions as following.

$E_w/C_w \leq 0.1$ corrosion dominant region.

$0.1 \leq E_w/C_w \leq 1$ corrosion–erosion region.

$1 \leq E_w/C_w \leq 10$ erosion–corrosion region.

$10 \leq E_w/C_w$ erosion dominant region.

Fig. 18 presents the erosion-corrosion map of Q235B steel at different flow velocities and temperatures. It is seen that all test points in this work locate in the region of erosion-corrosion, which means that the weight loss caused by the erosion and the corrosion is at the same order of magnitude and particularly the erosion loss is more significant than that caused by the corrosion. In addition, the ratios of E_w to C_w look stable without migration found for test points. Tables 7 and 8 indicate that the erosion enhanced the corrosion and the corrosion enhanced the erosion as well. Such interaction between erosion and corrosion causes flow erosion much different from pure erosion. E_c and C_e can be further analyzed to characterize the synergy effect.

Regions of erosion-corrosion can be defined depending whether the erosion-corrosion is "additive" or "synergistic" (Stack and Pungwiwat, 2004; Stack and Abd El Badia, 2006). The additive behavior and synergistic behavior can be divided into different regions as shown in the below (Yang and Cheng, 2012; Stack and Pungwiwat, 2004):

$E_c/E_0 \leq 1$ Low synergistic effect.

$1 \leq E_c/E_0 \leq 10$ medium synergistic effect.

$10 \leq E_c/E_0$ high synergistic effect.

$C_e/C_0 \leq 1$ low additive effect.

$1 \leq C_e/C_0 \leq 10$ medium additive effect.

$10 \leq C_e/C_0$ high additive effect.

The maps can also be used to show the affecting extent of temperature and flow velocity on the synergistic behavior and additive behavior. Fig. 19 (a) shows the diagram of the additive behavior, which is based on the ratio of erosion enhanced corrosion rate (C_e) and flow corrosion rate (C_0). It can be seen in Fig. 19a that with increasing flow velocity from 6 m/s to 11 m/s, the testing points are moved from low additive effect region to medium effect region and finally to the high additive effect region. This result indicates the flow velocity have strong positive effect on promoting the weight loss by increasing the rate of erosion enhanced corrosion. The additive behavior is also affected by the temperature.

From Fig. 19a, it can be found that the testing points are moved from the medium additive effect region to the low additive effect region when the temperature is increased, which indicates the influence of temperature on additive behavior is weakened. The possible reason is that the increase of flow corrosion rate C_0 is much greater than that of erosion enhanced corrosion (C_e) when temperature is increased as shown in Table 8, due to the high sensitive of corrosion rate to temperature.

Fig. 19b is the diagram of the synergistic behavior, which bases on the ratio of corrosion enhanced erosion rate (E_c) and pure erosion rate (E_0). It can be seen in Fig. 19b that most of the points are located at the medium synergistic effect region at different flow velocities. The testing points of different temperatures are located at the medium synergistic region as well, but there is a trend of moving from medium synergistic region to high synergistic region. It is reasonable because the pure erosion rate (E_0) is not sensitive to the change of temperature (Molkens et al., 2021), but corrosion enhanced erosion (E_c) is promoted by severe corrosion at high temperature, as shown in Table 8.

From the analysis of erosion-corrosion components, the influences of flow velocity and temperature on the components under erosion-corrosion condition is discussed as follows: Both high velocity and high temperature have positive effects on total erosion-corrosion rate (T). The main source of weight loss rates of Q235B steel is the total erosion rate (E_w), which includes the pure erosion rate (E_0) and the corrosion enhanced erosion rate (E_c). The corrosion enhanced erosion rate (E_c) is essential to synergy, which is consistent with the results from other researchers (Shahali et al., 2019; Abedini and Ghasemi, 2014).

4. Conclusions

(1) The weight loss rates of specimens caused by erosion-corrosion increase with increasing flow velocity and temperature. The flow velocity has small effect directly on the weight loss rate caused by corrosion, and temperature almost has no effect on the weight loss rate caused by pure erosion.

(2) From electrochemical measurement, it is found that the corrosion of the specimen becomes severer when the temperature is increased due to reducing the activation energy. Under erosion-corrosion process, the corrosion rates of specimens increase with increasing flow velocity due to the

enhancement of interaction between erosion and corrosion. However, under the flow corrosion condition, the corrosion rates of specimens decrease with increasing flow velocity, possibly due to the stagnant zone in the flow field.

(3) The results of surface morphology show that some larger circular corrosion pits are formed on the surface of the specimens at high temperature (30 °C and 40 °C), which indicates the increase of temperature could promote the deterioration of localized corrosion. Under the effect of high flow velocity, the localized corrosion pits could no longer remain the circular shape, which means the corrosion pattern might tend to become uniform corrosion as flow velocity is increased.

(4) For erosion-corrosion of Q235B steel, synergy is the main reason for causing material loss and corrosion enhanced erosion rate is the dominant component in synergy. In the analysis of regimes of erosion-corrosion, the results indicate that "additive" effect becomes more significant with increasing flow velocity, while it is weakened when the temperature is increased. The synergistic effect is not sensitive to the changes of flow velocity and temperature.

Acknowledgements

References

Abedini, M., Ghasemi, H.M., 2014. Synergistic erosion–corrosion behavior of Al–brass alloy at various impingement angles. Wear 319 (1–2), 49–55. https://doi.org/10.1016/j.wear.2014.07.008.

Aguirre, J., Walczak, M., 2018. Multifactorial study of erosion–corrosion wear of a X65 steel by slurry of simulated copper tailing. Tribol. Int. 126, 177–185. https://doi.org/10.1016/j.triboint.2018.04.029.

Aguirre, J., Walczak, M., Rohwerder, M., 2019. The mechanism of erosion-corrosion of API X65 steel under turbulent slurry flow: effect of nominal flow velocity and oxygen content. Wear 438–439. https://doi.org/10.1016/j.wear.2019.203053, 203053.

Alam, T., Aminul, I.M., Farhat, Z.N., 2016. Slurry erosion of pipeline steel: effect of velocity and microstructure. J. Tribol. 138, 021604. https://doi.org/10.1115/1.4031599.

Amin, M.A., Abd El-Rehim, S.S., El-Sherbini, E.E.F., Bayoumi, R.S., 2007. The inhibition of low carbon steel corrosion in hydrochloric acid solutions by succinic acid. Electrochim. Acta 52 (11). https://doi.org/10.1016/j.electacta.2006.10.019, 3588-00.

Anderson, S.L., Longmire, E.K., 1995. Particle motion in the stagnation zone of an impinging air jet. J. Fluid Mech. 299, 333–366. https://doi.org/10.1017/S0022112095003521.

Denny, A.J., 1996. In: Principles and Prevention of Corrosion, second ed. Prentice Hall, New York.

Elemuren, R., Evitts, R., Oguocha, I.N.A., Kennell, G., Gerspacher, R., Odeshi, A.G., 2020. Full factorial, microscopic and spectroscopic study of erosion-corrosion of AISI 1018 steel elbows in potash brine-sand slurry. Tribol. Int. 142, 105989. https://doi.org/10.1016/j.triboint.2019.105989.

Guo, H.X., Lu, B.T., Luo, J.L., 2005. Interaction of mechanical and electrochemical factors in erosion–corrosion of carbon steel. Electrochim. Acta 51 (2), 315–323. https://doi.org/10.1016/j.electacta.2005.04.032.

Guo, L., Zhang, R., Tan, B., Li, W.P., Liu, H.Y., Wu, S.Z., 2020. Locust Bean Gum as a green and novel corrosion inhibitor for Q235 steel in 0.5 M H_2SO_4 medium. J. Mol. Liq. 310, 113239. https://doi.org/10.1016/j.molliq.2020.113239.

Hirata, R., Ooi, A., Tada, E., Tada, E., Nishikata, A., 2021. Influence of the degree of saturation on carbon steel corrosion in soil. Corrosion Sci. 189, 109568. https://doi.org/10.1016/j.corsci.2021.109568.

Islam, M.A., Farhat, Z.N., 2014. Effect of impact angle and velocity on erosion of API X42 pipeline steel under high abrasive feed rate. Wear 311 (1–2), 180–190. https://doi.org/10.1016/j.wear.2014.01.005.

Javaheri, V., Porter, D., Kuokkala, V.T., 2018. Slurry erosion of steel - review of tests, mechanisms and materials. Wear 408–409, 248–273. https://doi.org/10.1016/j.wear.2018.05.010.

Kalifa, R.B., Habli, S., Saïd, N.M., Bournot, H., Le Palec, G., 2016. Parametric analysis of a round jet impingement on a heated plate. Int. J. Heat Fluid Flow 57, 11–23. https://doi.org/10.1016/j.ijheatfluidflow.2015.11.005.

Karafyllias, G., Galloway, A., Humphries, E., 2019. The effect of low pH in erosion-corrosion resistance of high chromium cast irons and stainless steels. Wear

420–421, 79–86. https://doi.org/10.1016/j.wear.2018.11.021.

Kim, Y.J., Kim, S.W., Kim, H.B., Park, C.N., Choi, Y.I., Park, C.J., 2019. Effects of the precipitation of secondary phases on the erosion-corrosion of 25% Cr duplex stainless steel. Corrosion Sci. 152, 202–210. https://doi.org/10.1016/j.corsci.2019.03.006.

Laukkanen, A., Lindgren, M., Andersson, T., Pinomaa, T., Lindroos, M., 2020. Development and validation of coupled erosion-corrosion model for wear resistant steels in environments with varying pH. Tribol. Int. 151, 106534. https://doi.org/10.1016/j.triboint.2020.106534.

Li, L.L., Wang, Z.B., Zheng, Y.G., 2019. Interaction between pitting corrosion and critical flow velocity for erosion-corrosion of 304 stainless steel under jet slurry impingement. Corrosion Sci. 158, 108084. https://doi.org/10.1016/j.corsci.2019.07.008.

Liu, M., Yao, J., Zhao, Y.L., 2021. The dispersion of particles in turbulent semi-circular duct flows. Petrol. Sci. 18 (4), 1240–1255. https://doi.org/10.1016/j.petsci.2021.05.004.

Liu, Y., Zhao, Y.L., Yao, J., 2021. Synergistic erosion–corrosion behavior of X80 pipeline steel at various impingement angles in two-phase flow impingement. Wear 466–467, 203572. https://doi.org/10.1016/j.wear.2020.203572.

Lu, B.T., Lu, J.F., Luo, J.L., 2011. Erosion–corrosion of carbon steel in simulated tailing slurries. Corrosion Sci. 53 (3), 1000–1008. https://doi.org/10.1016/j.corsci.2010.11.034.

Mahdi, E., Rauf, A., Eltai, E.O., 2014. Effect of temperature and erosion on pitting corrosion of X100 steel in aqueous silica slurries containing bicarbonate and chloride content. Corrosion Sci. 83, 48–58. https://doi.org/10.1016/j.corsci.2014.01.021.

Mccafferty, E., 1990. A competitive adsorption model for the inhibition of crevice corrosion and pitting. J. Electrochem. Soc. 137, 3731–3737. https://iopscience.iop.org/article/10.1149/1.2086294.

Molkens, T., Cashell, K.A., Rossi, B., 2021. Post-fire mechanical properties of carbon steel and safety factors for the reinstatement of steel structures. Eng. Struct. 234, 111975. https://doi.org/10.1016/j.engstruct.2021.111975.

Owen, J., Ramsey, C., Barker, R., Neville, A., 2018. Erosion-corrosion interactions of X65 carbon steel in aqueous CO_2 environments. Wear 414–415, 376–389. https://doi.org/10.1016/j.wear.2018.09.004.

Rajahram, S.S., Harvey, T.J., Wood, R.J.K., 2009. Evaluation of a semi-empirical model in predicting erosion–corrosion. Wear 267 (11), 1883–1893. https://doi.org/10.1016/j.wear.2009.03.002.

Rameshk, M., Soltanieh, M., Masoudpanah, S.M., 2020. Effects of flow velocity and impact angle on erosion-corrosion of an API-5 L X65 steel coated by plasma nitriding of hard chromium underlayer. J. Mater. Res. Technol. 9 (5), 10054–10061. https://doi.org/10.1016/j.jmrt.2020.07.013.

Sasaki, K., Burstein, G.T., 2000. Observation of a threshold impact energy required to cause passive film rupture during slurry erosion of stainless steel. Phil. Mag. Lett. 80, 489–493. https://doi.org/10.1080/09500830050057198.

Shahali, H., Ghasemi, H.M., Abedini, M., 2019. Contributions of corrosion and erosion in the erosion-corrosion of Sanicro28. Mater. Chem. Phys. 233, 366–377. https://doi.org/10.1016/j.matchemphys.2019.05.051.

Slemnik, M., 2016. Activation energies ratio as corrosion indicator for different heat treated stainless steels. Mater. Des. 89. https://doi.org/10.1016/j.matdes.2015.10.035, 795-01.

Stack, M.M., Abd El Badia, T.M., 2006. Mapping erosion–corrosion of WC/Co–Cr based composite coatings: particle velocity and applied potential effects. Surf. Coating. Technol. 201 (3–4), 1335–1347. https://doi.org/10.1016/j.surfcoat.2006.01.069.

Stack, M.M., Corlett, N., Turgoose, S., 2003. Some thoughts on modelling the effects of oxygen and particle concentration on the erosion–corrosion of steels in aqueous slurries. Wear 255 (1–6), 225–236. https://doi.org/10.1016/s0043-1648(03)00205-9.

Stack, M.M., Pungwiwat, N., 2002. Particulate erosion–corrosion of Al in aqueous conditions: some perspectives on pH effects on the erosion–corrosion map. Tribol. Int. 35 (10), 651–660. https://doi.org/10.1016/S0301-679X(02)00056-7.

Stack, M.M., Pungwiwat, N., 2004. Erosion–corrosion mapping of Fe in aqueous slurries: some views on a new rationale for defining the erosion–corrosion interaction. Wear 256 (5), 565–576. https://doi.org/10.1016/s0043-1648(03)00566-0.

Tummers, M.J., Jacobse, J., Voorbrood, S.G.J., 2011. Turbulent flow in the near field of a round impinging jet. Int. J. Heat Mass Tran. 54 (23–24), 4939–4948. https://doi.org/10.1016/j.ijheatmasstransfer.2011.07.007.

Wang, Z.B., Zheng, Y.G., Yi, J.Z., 2019. The role of surface film on the critical flow velocity for erosion-corrosion of pure titanium. Tribol. Int. 133, 67–72. https://doi.org/10.1016/j.triboint.2019.01.006.

Wood, R.J.K., 2006. Erosion–corrosion interactions and their effect on marine and offshore materials. Wear 261 (9), 1012–1023. https://doi.org/10.1016/j.wear.2006.03.033.

Xia, D.-H., Ma, C., Behnamian, Y., Ao, S.S., Song, S.Z., Xu, L.K., 2019. Reliability of the estimation of uniform corrosion rate of Q235B steel under simulated marine atmospheric conditions by electrochemical noise (EN) analyses. Measurement 148, 106946. https://doi.org/10.1016/j.measurement.2019.106946.

Xu, Y., Liu, L., Zhou, Q., Wang, X.N., Huang, Y., 2020. Understanding the influences of pre-corrosion on the erosion-corrosion performance of pipeline steel. Wear 442–443. https://doi.org/10.1016/j.wear.2019.203151, 203151.

Xu, Y., Tan, M.Y., 2019. Probing the initiation and propagation processes of flow accelerated corrosion and erosion corrosion under simulated turbulent flow conditions. Corrosion Sci. 151, 163–174. https://doi.org/10.1016/

j.corsci.2019.01.028.

Yang, Y., Cheng, Y.F., 2012. Parametric effects on the erosion–corrosion rate and mechanism of carbon steel pipes in oil sands slurry. Wear 276–277, 141–148. https://doi.org/10.1016/j.wear.2011.12.010.

Yao, J., Zhou, F., Zhao, Y.L., Yin, H., Li, N., 2015. Investigation of erosion of stainless steel by two-phase jet impingement. Appl. Therm. Eng. 88, 353–362. https://doi.org/10.1016/j.applthermaleng.2014.08.056.

Zhang, C., Zhu, H., Zhu, L., 2021. Effect of interaction between corrosion and high temperature on mechanical properties of Q355 structural steel. Construct. Build. Mater. 271, 121605. https://doi.org/10.1016/j.conbuildmat.2020.121605.

Zhao, Y.L., Tang, C.Y., Yao, J., Zeng, Z.H., Dong, S.G., 2020. Investigation of erosion behavior of 304 stainless steel under solid-liquid jet flow impinging at 30. Petrol. Sci. 17, 1135–1150. https://doi.org/10.1007/s12182-020-00473-7.

Zhao, Y.L., Zhou, F., Yao, J., Dong, S.G., Li, N., 2015. Erosion–corrosion behavior and corrosion resistance of AISI 316 stainless steel in flow jet impingement. Wear 328–329, 464–474. https://doi.org/10.1016/j.wear.2015.03.017.